Journal of Materials Chemistry A

ROYAL SOCIETY OF CHEMISTRY

PAPER

View Article Online
View Journal | View Issue

Cite this: J. Mater. Chem. A, 2024, 12, 7777

Exposing the (002) active facet by reducing surface energy for a high-performance $Na_3V_2(PO_4)_2F_3$ cathode†

Zhuangzhi Li, [a] Lang Qiu,[a] Ping Li,[a] Hao Liu,[b] Dong Wang,[c] Weibo Hua, [d] Ting Chen,[e] Yang Song, [af] Fang Wan, [a] Benhe Zhong,[a] Zhenguo Wu [*a] and Xiaodong Guo [*a]

Increasing the exposure of active crystal facets is an effective strategy to promote the transmission of Na^+ through the electrolyte/cathode interface and is key to developing high-performance sodium-ion battery (SIB) cathodes. Here, $Na_3V_2(PO_4)_2F_3$ (NVPFs) were synthesized with diverse (002) active facet exposure rates, in which the growth rate of the different crystal facets was regulated by adjusting the surface energy. The growth mechanism of the NVPF crystals was proposed using density functional theory calculations. The NVPFs with 82% (002) active facet exposure delivered a remarkable reversible capacity of 123 mA h g^{-1} and energy density of 431 W h kg^{-1} in a full cell. Theoretical investigations of the Na^+ adsorption, diffusion, and storage clarified that the exposed (002) crystal facet had more stable Na^+-storage sites, which resulted in a lower energy barrier during the Na^+-diffusion process. The promoted Na^+-transportation kinetics and related enhanced stability were further elucidated based on the combined analyses of synchrotron X-ray absorption spectroscopy and electrochemical measurements. This research aimed to develop a way to promote the transmission process of Na^+ through the electrolyte/cathode interface from the perspective of crystal facet regulation, which is expected to promote the commercial application of SIB cathodes.

Received 22nd December 2023
Accepted 5th February 2024

DOI: 10.1039/d3ta07954f

rsc.li/materials-a

Introduction

The rise in the grid energy-storage battery market has accelerated the demand for sodium-ion batteries (SIBs), especially SIBs with high energy density, high power density, low cost, and a long cycle life.[1–8] Substantial efforts have been devoted to developing and optimizing high-performance electrode materials for SIBs, especially cathode materials, to promote the commercialization of SIBs.[9–14] Among the many developed cathode materials for SIBs, polyanion compounds, especially phosphate compounds and fluorophosphate phase compounds belonging to sodium superionic conductors (NASICONs), have attracted extensive interest due to their strong phosphate-metal bonds and stable three-dimensional framework structure, resulting in thermal stability and long lifespans.[15–18] However, their inherent low conductivity limits their further application.[3,19–25] The electrochemical reaction process of sodium ions (Na^+) in the SIB on the cathode side can usually be described as follows: first, Na^+ desolvates from the electrolyte and diffuses to the electrolyte/cathode interface; then, the Na^+ enters the cathode material through this interface, and finally it diffuses in the cathode material. During the process of de-insertion, Na^+ goes retrograde along the pathway mentioned above. [26–28] The first step above is mainly determined by the electrolyte properties, while the next two steps mainly depend on the properties of the cathode material. Therefore, for developing high-performance cathode materials, efforts should be aimed at promoting the transport process of Na^+ through the electrolyte/cathode interface or enhancing the high-speed diffusion process of Na^+ within the cathode structure.

The Na^+ exchange between the electrolyte and cathode materials occurs at the crystal facets of cathode materials. The crystal facet structure of cathodes intrinsically determines the adsorption and desorption of reactants (including Na^+) and the charge transfer between the reactants on the crystal facets.

[a]School of Chemical Engineering, Sichuan University, Chengdu, 610065, China. E-mail: xiaodong2009@163.com; zhenguowu@scu.edu.cn
[b]Institute for Applied Materials (IAM), Karlsruhe Institute of Technology (KIT), Hermann-von-Helmholtz-Platz 1, Eggenstein-Leopoldshafen, 76344, Germany
[c]College of Materials Science and Engineering, Chongqing University, Chongqing 400030, China
[d]School of Chemical Engineering and Technology, Xi'an Jiaotong University, Xi'an, 710049, China
[e]Institute for Advanced Study, Chengdu University, Chengdu, 610106, China
[f]Chemistry and Chemical Engineering Guangdong Laboratory, Shantou, 515041, China

† Electronic supplementary information (ESI) available: Additional results (XRD Rietveld refinements results, SEM and TEM images, XPS spectra, parameters of c-cluster, surface energy, electrochemical performance, *K*-space), supporting Text (GITT calculation method). See DOI: https://doi.org/10.1039/d3ta07954f

Therefore, the performances of cathode materials rely on the crystal facets exposed to the electrolyte. In view of this, compared with modification methods such as coating and doping, increasing the exposure of active facets is considered a more effective strategy to improve the performance of cathode materials.[29,30] Our previous work showed that exposing advantageous crystal facets could promote the performance of materials, and so we synthesized cathode materials with different crystal facets exposed by doping metal ions, adjusting the pH, and changing the stirring speed.[31–33] In other studies, excellent performance has also been achieved through crystal facet regulation.[34–39]

Based on the above, in this work, we synthesized $Na_3V_2(PO_4)_2F_3$ (NVPFs) with different (002) active facet exposure rates, which could regulate the growth rate of the different crystal facets by regulating the surface energy using carbon clusters (c-clusters) as inducers. The growth mechanism of NVPF crystals with or without c-cluster adsorption was proposed using density functional theory (DFT) calculations. The NVPFs with more (002) crystal facets exposed (NVPF-(002)) delivered a remarkable reversible capacity of 123 mA h g^{-1} and energy density of 431 W h kg^{-1} in a full cell. First-principle calculations were performed for the Na^+ adsorption, diffusion, and storage of NVPFs to clarify the Na^+-storage sites and the energy barriers for the different exposed crystal facets. Further, synchrotron X-ray absorption spectroscopy (XAS) and electrochemical mechanism analysis were performed to elucidate the essence of the performance differences of the NVPFs.

Results and discussion

The phase confirmations of NVPF-(002) and pure-NVPFs (NVPF) were characterized and analyzed by synchrotron radiation X-ray diffraction (SRXRD), Fourier transform infrared (FTIR) spectroscopy, and Raman spectroscopy. As shown in Fig. 1a and b, the SRXRD patterns of the synthesized samples accorded with the tetragonal structure (ICDD No. 04-012-2207), with weak signals from the raw material VPO_4, indicating that the NVPFs were successfully synthesized through the hydrothermal method. The refined fitting line matched the measurement results, with the crystallographic data obtained through refinement listed in Tables S1–S3.† The agreement factors and small differences in the plots indicated that the refined results were highly reliable. Also, the cell parameters of NVPF-(002) (a = 9.04653 Å, c = 10.74423 Å) were similar to those of NVPF (a = 9.04549 Å, c = 10.74936 Å). The phase compositions of the two samples were obtained through refinement (Fig. 1c), with $Na_3V_2(PO_4)_2F_3$ contents of 99.0 wt% for NVPF-(002) and 97.2 wt% for NVPF, respectively. Additional diffraction peaks came from the incompletely converted raw material VPO_4, with a 1 wt% content for NVPF-(002) and 2.8 wt% for NVPF, respectively. The FTIR characterization results in Fig. 1d further confirmed the composition of the synthesized material. The vibrations observed in the 500–700 cm^{-1} region could be attributed to the bending mode of P–O in PO_4.[40–42] The signal at 940 cm^{-1} corresponded to the vibration band of V–F, and no vibration band belonging to V=O was observed at 900 cm^{-1}.[11,40,42–45] In addition, a strong large band (950–1150 cm^{-1}) appeared, consisting of several vibrations of PO_4.[40–44] The Raman spectra of the two samples are shown in Fig. 1e, with peaks appearing at the same positions and similar shapes and relative intensities. The peak at 300 cm^{-1} belonged to the ν_2 mode, which was caused by external vibration caused by PO_4 and V–O vibrations. The remaining Raman peaks were assigned to the vibrations of the three internal modes of tetrahedral PO_4. The two bands at 520 and 575 cm^{-1} were ascribed to ν_4 vibration, while the bands at

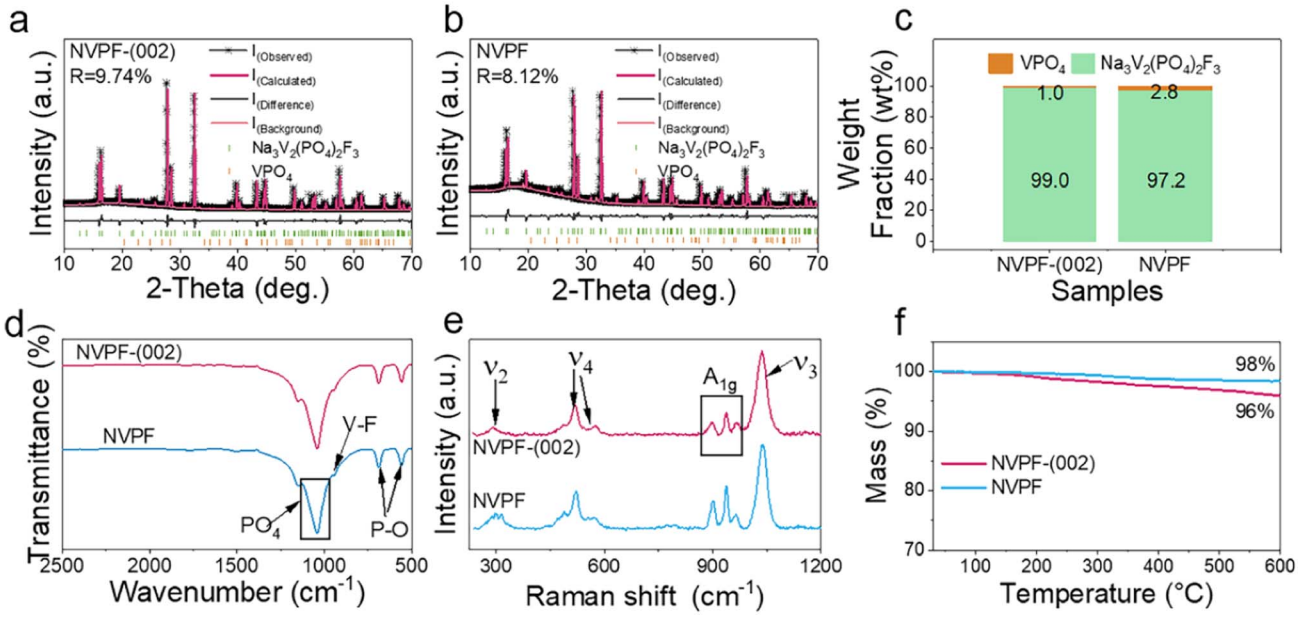

Fig. 1 Rietveld refinement of the synchrotron radiation X-ray diffraction patterns of (a) NVPF-(002) and (b) NVPF. (c) Phase compositions, (d) FTIR spectra, (e) Raman spectra, and (f) TG curves of NVPF-(002) and NVPF.

935 and 900 cm^{-1} could be attributed to the A_{1g} symmetric P–O stretching vibration bands of ν_1, and the higher band at 1035 cm^{-1} was attributed to the antisymmetric stretching band of the PO_4 anion (ν_3).[46,47] Thermogravimetric analysis (TGA) was used to characterize the mass changes of the two samples from 30 °C to 600 °C in a nitrogen atmosphere at a heating rate of 5 °C min^{-1}. As shown in Fig. 1f, the mass of NVPF-(002) decreased by 4% with increasing the temperature, which was consistent with the carbon content (4.15 wt%) obtained by the elemental analyzer. Therefore, the decrease in mass was related to carbon decomposition. The mass of NVPF hardly changed, with a loss rate of only 2%.

The morphology of the two samples was characterized by field emission scanning electron microscopy (FESEM). The results show that the particle morphology of the two samples was a rectangular cuboid sheet, with the two samples showing different thicknesses of sheets (Fig. S1†). As shown in Fig. 2a and b, the thickness of the NVPF-(002) sample was clearly much thinner than that of the NVPF sample. The thickness contrast in transmission electron microscopy (TEM) images can usually be used to qualitatively compare the thicknesses of samples.[48] The TEM images show morphologies as in the FESEM images. Fig. 2c and d further confirmed that the thickness of the NVPF-(002) sample was thinner than that of the NVPF sample. The particle statistical average thicknesses and length/thickness ratios of the NVPF-(002) and NVPF samples were 327 nm and 9.37, and 774 nm and 3.96, respectively (Fig. 2e and f). These results demonstrated that cathodes with different length/thickness ratios could be obtained by introducing/not introducing c-clusters. Further, the difference in the morphology of the cathodes determined the proportion of facets exposed to the electrolyte.

The crystal facet exposure of the NVPFs was determined by TEM and selected area electron diffraction (SAED) characterization. Fig. 2g shows the particle morphology obtained by TEM, while Fig. 2h shows the electron diffraction pattern of the selected area in Fig. 2g. The SAED patterns of the NVPFs well matched the [002] zone axis projection of the tetragonal $P4_2/mnm$ space group (Fig. 2h and S2b†). The diffraction pattern obtained from characterization in Fig. 2h is consistent with the simulated diffraction pattern in Fig. S2c,† without additional spots. Through comprehensive analysis of the morphology image and electron diffraction patterns, it was determined that the top (bottom) surface of the particles corresponded to the (002) facets and the side surface corresponded to the (220) facets. The exposure ratios of the (002) facets and (220) facets

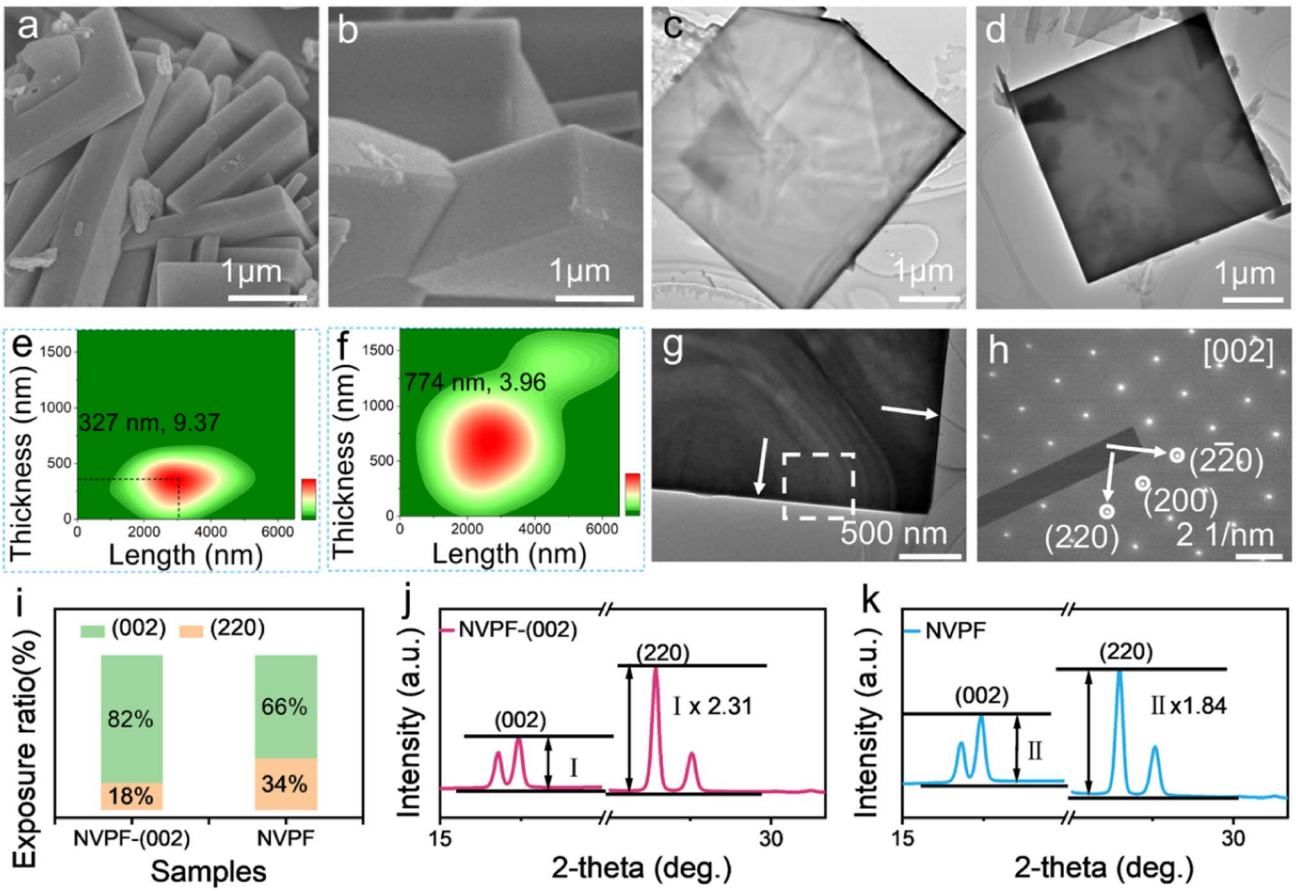

Fig. 2 SEM images of (a) NVPF-(002) and (b) NVPF. TEM images of (c) NVPF-(002) and (d) NVPF. Statistical diagrams of the particle length and thickness for (e) NVPF-(002) and (f) NVPF. (g) Surface TEM image. (h) SAED pattern. (i) Exposure area ratio of the (002) and (220) crystal facets. The intensity ratio of the (002) peak to the (220) peak for (j) NVPF-(002) and (k) NVPF.

were quantified by combining the average thickness and length of the particles. The detailed analysis method for determining the crystal facet exposure ratio is described in supporting Text 1.† The proportions of (002) facets and (220) facets in the NNVPF-(002) sample and NVPF sample to the total exposed surface were 82% and 18%, and 66% and 34%, respectively, indicating that the introduction of c-clusters altered the exposure ratio of the NVPFs' facets. In the same volume of cathode particles, the exposure area of the (002) facets in the NVPF-(002) sample was 2.36 times that of the NVPF sample. The performances of compounds exposed to different facets usually vary, and similar situations also exist in the cathode.[31,32,36,37,39–51] Fig. 2j and k show the SRXRD patterns of the as-prepared NVPFs at 15°–31°. After the introduction of c-clusters, the ratio of $I_{(220)}/I_{(002)}$ increased from 1.84 to 2.31, further confirming the transformation of the particle growth direction. A stronger (220) peak indicated that the crystal cell preferentially grew along the [110] axis perpendicular to the (220) facet, while a weaker (002) diffraction peak indicated the slower growth along the [001] axis perpendicular to the (002) facet, which exposed more of the (002) facet.[49]

The properties of a crystal itself are the internal factors that determine its growth process and final morphology. The external environment in which it grows also significantly influences its morphology. The same crystal could a have different morphology in different environments. The presence of impurities or foreign matter can change the surface energy of different facets of the crystal, so the growth rate of varying facets will also change, thus changing the particle morphology.[52–54] It is generally accepted that the differences in crystal morphology are mainly due to the anisotropic growth process of the crystal. During this process, the growth rate of high-energy surfaces in materials is higher than that of low-energy surfaces, resulting in a preferred growth orientation in the direction of the high-energy surface of the material.[55] Here, DFT calculations were used for investigate the growth process of crystals and the factors influencing their morphology differentiation. The surface energies of the (001) crystal facet and (110) crystal facet, and the adsorption energies of these facets absorbed by the c-cluster were selected for further analysis based on the results in Fig. 2. The establishment of the c-cluster was done based on the X-ray photoelectron spectroscopy (XPS) results (Fig. S4†). Fig. S5† shows the atomic structure of the c-cluster in the side and top views, and Table S5† shows the atomic coordinates and structure parameters. The exposed layers corresponding to the same crystal cell and crystal facet were different, so it was necessary to optimize the models corresponding to different exposed layers, and to select stable and low-energy exposed layers to adsorb adsorbates. For the (001) crystal facet, there were two types of exposed layers, as shown in Fig. 3a, namely Na–F terminated and V–P terminated, respectively; while for the (110) crystal facet, as shown in Fig. 3b, these were Na–O terminated and V–P–O terminated, respectively. The total energy (E_{tot}) of the model was compared, and the results showed that the E_{tot} of the Na–F terminated layer was smaller than the E_{tot} of the V–P terminated layer in the two models for the (001) crystal facet (Fig. 3a). This indicated that the Na–F terminated layer was more stable, so the (002) crystal facet in the NVPF crystals was more inclined to expose the Na–F layer. In the model of the (110) crystal facet, the E_{tot} of the Na–O terminated layer was lower than the E_{tot} of the V–P–O terminated layer. Therefore, the (220) crystal facet in the NVPF crystal was more inclined to expose the Na–O layer (Fig. 3b). The surface energy results also supported the above results, and the corresponding results are summarized in Table S6.† The surface energy of the Na–F terminated layer was smaller than that of the V–P terminated layer in the two models for the (001) crystal facet (Fig. 3c). The surface energy of the Na–O terminated layer was smaller than that of the V–P–O terminated layer in the two models of the (001) crystal facet (Fig. 3d). Based on the above results, models were established for the adsorption of the exposed layer and c-cluster, and the structure was fully optimized. The system total energy after the adsorption of the exposed layer and c-cluster was calculated *via* DFT, as shown in Fig. 3e. The results indicated that the energy of the system adsorbed by c-cluster on the (001) crystal facet was lower and therefore more stable. Generally, a more negative adsorption energy means a stronger adsorption process.[56–59] The adsorption energy calculation results showed that the adsorption energy on the (001) crystal facet (−4.3 eV) was greater than that on the (110) crystal facet (−3.71 eV), so the c-cluster was more inclined to adsorb on the (001) facet (Fig. 3f). As shown in Fig. 3h, the result from the above factors was that the growth on the (002) facets was hindered due to the adsorption of c-clusters, which could reduce the surface energy and generate two-dimensional particles. By contrast, the NVPF crystals that were not affected by c-clusters grew along three dimensions, as the (001) and (110) facets had a similar surface energy (Fig. 3g and i). Diverse growth methods resulted in NVPFs with different facet exposures, as indicated by the previous SEM, TEM, and SAED results.

Electrochemical measurements were conducted at room temperature (30 °C) and at low temperature (−20 °C) using the NVPFs as cathodes to explore the electrochemical performance of the NVPFs with diverse facet exposure ratios. As the contact interface of the cathode facets/electrolytes was different in each case, the cathodes exhibited different electrochemical behaviors. Fig. 4a shows the rate capabilities at different current densities ranging from 0.1 to 5C of the two cathodes at room temperature. The initial specific capacity was higher than the theoretical specific capacity (128 mA h g^{-1}), which may have been due to the additional capacity from the use of Ketjenblank (KB) (Fig. S6†), and this extra capacity has also been reported in other fluorophosphate-based SIBs cathodes.[10,60] NVPF-(002) delivered a much better rate capability at each rate. The corresponding detailed electrochemical test results are comprehensively summarized in Table S7.† In particular, the NVPF-(002) cathode could provide a specific capacity of 98 mA h g^{-1} and an energy density of 338 W h kg^{-1} even at a high rate of 5C and a corresponding power density up to 2123 W kg^{-1}, whereas the specific capacity of the NVPF cathode was merely 58 mA h g^{-1} and the energy density was 175 W h kg^{-1}. The rate curve results showed that as the charge/discharge current increased, the NVPF-(002) cathode with more (002) facet exposure could provide more reversible capacity. The corresponding charge/

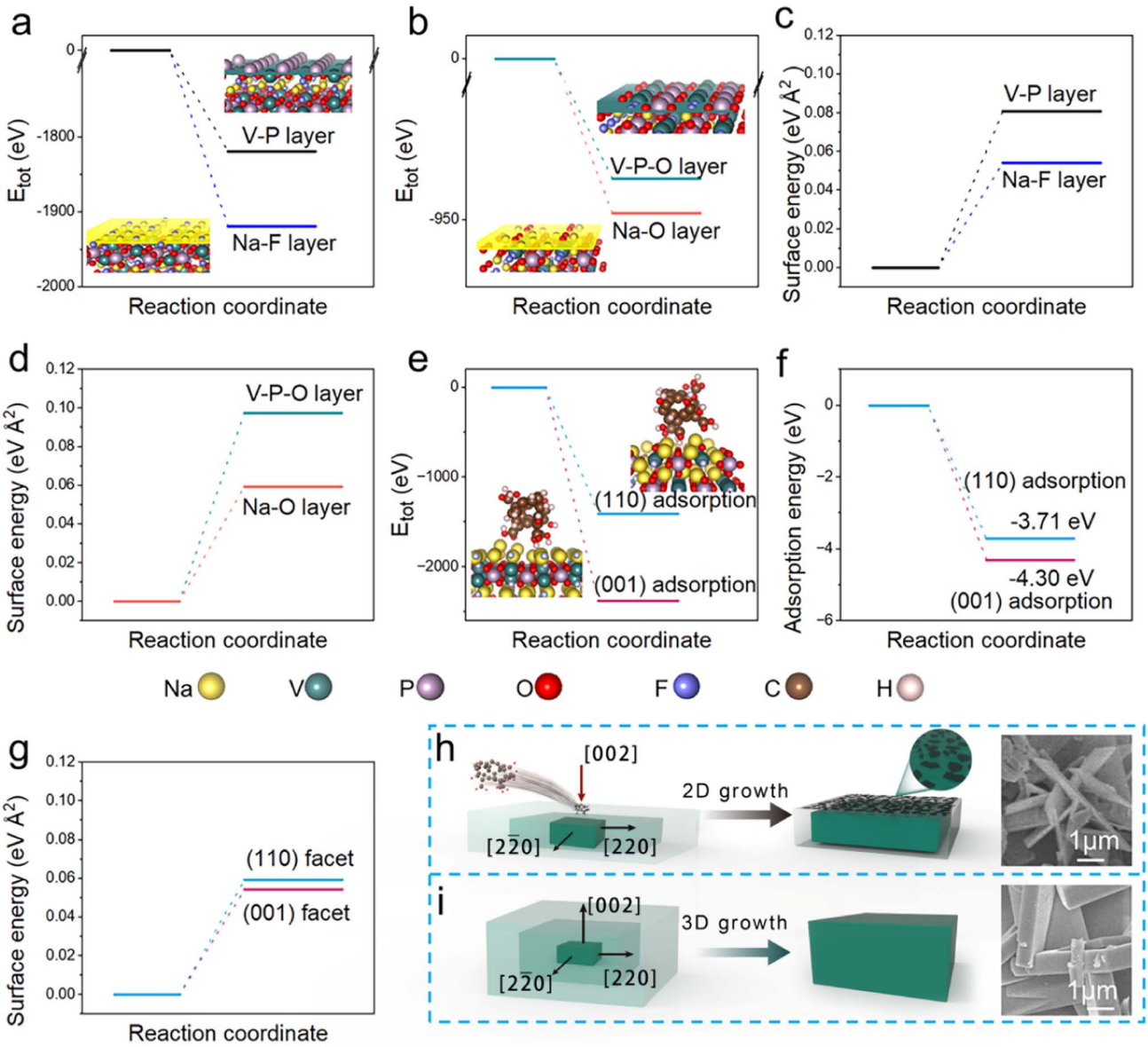

Fig. 3 Comparison of the total energy and surface energy for: the exposed layer (a) and (c) Na–F termination and V–P termination of the (001) crystal facet; (b) and (d) Na–O termination and V–P–O termination of the (110) crystal facet. (e) Schematic diagram of the (001) crystal facet adsorption of the c-cluster and the (110) plane adsorption of the c-cluster, comparison of system total energy. (f) Comparison of the adsorption energy. (g) Comparison of surface energy between the clean (001) facet and (110) facet. Schematic diagram of the growth: (h) NVPF-(002) sample, (i) NVPF sample.

discharge curves at different rates further confirmed the advantages of the NVPF-(002) cathode, which could provide high capacity while maintaining a higher discharge voltage (Fig. 4b). The above results indicate that the NVPF-(002) cathode had higher energy density, and this advantage became more apparent with the increase in current density, which is intuitively presented in the energy density–power density plots (Ragone plots) in Fig. 4c. Fig. 4d shows the cycle performances of the NVPF-(002) cathode and NVPF cathode at 2C. The initial discharge specific capacities of the NVPF-(002) cathode and NVPF cathode were 124 and 110 mA h g^{-1}, respectively. After 1400 cycles, the capacities were 111 and 85 mA h g^{-1}, respectively, with capacity retention rates of 89% and 77%. The discharge mass energy densities of the NVPF-(002) cathode and NVPF cathode were 432 and 368 W h kg^{-1}, respectively. After 1400 cycles, the capacities were 391 and 280 W h kg^{-1}, respectively, with retention rates of 90% and 76%. The two cathodes thus showed remarkable stability during long-term charge–discharge tests, but the reversible discharge specific capacity and energy density of the NVPF-(002) cathode were always higher than those of the NVPF cathode, and the energy efficiency was also higher than that of the NVPF cathode (Fig. S7†). To further evaluate the rate performance and cycling stability, the cells were placed in a low-temperature environment of −20 °

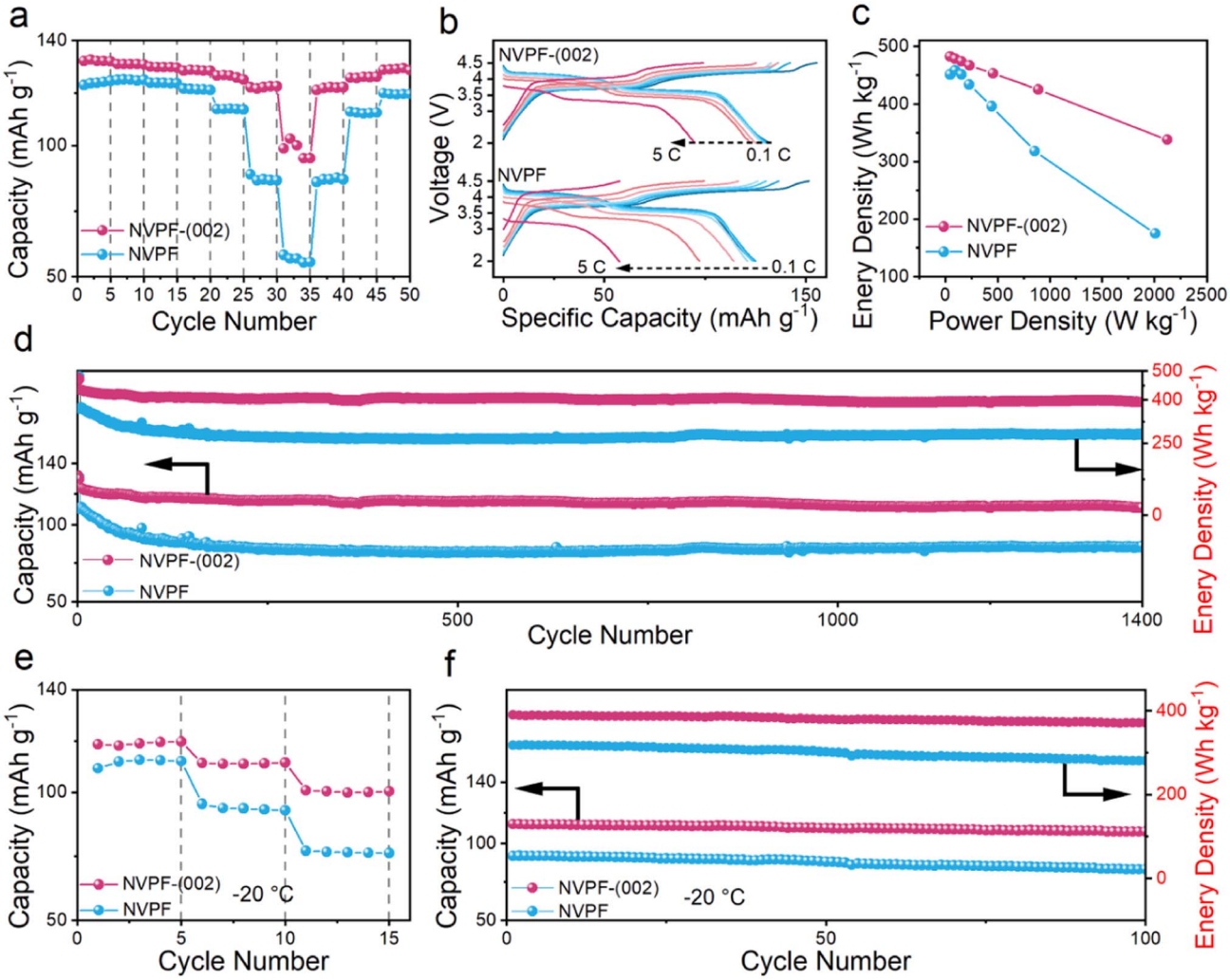

Fig. 4 Electrochemical measurements at room temperature (30 °C): (a) rate performance comparison of NVPF cathodes at 0.1C, 0.2C, 0.3C, 0.5C, 1C, 2C, and 5C. (b) Corresponding charge–discharge curves. (c) Corresponding Ragone plots. (d) Cycle performance of NVPF-(002) cathode and NVPF cathode at 2C. Electrochemical measurements at low temperature: (e) rate performance comparison of NVPF cathodes at 0.1C, 0.2C, and 0.3C. (f) Cycle performance of NVPF-(002) cathode and NVPF cathode at 0.2C.

C for charge–discharge testing. The NVPF-(002) cathode showed discharge specific capacities of 119, 111, and 100 mA h g^{-1} at rates of 0.1C, 0.2C, and 0.3C, respectively; whereas the discharge specific capacities of the NVPF cathode at rates of 0.1C, 0.2C, and 0.3C were only 109, 95, and 77 mA h g^{-1}, respectively. As expected, the NVPF-(002) cathode exhibited better rate performance (Fig. 4e). As shown in Fig. 4f, the long cycle test results at low temperature were similar to those at room temperature, with both cathodes exhibiting good cycle stability, but the NVPF-(002) cathodes could provide a higher specific capacity and energy density than NVPF. In summary, whether at room temperature or low temperature, the NVPF-(002) cathode provided higher reversible capacity and energy density. Moreover, as the current density increased, the difference in capacity and energy density between the NVPF-(002) cathode and the NVPF cathode became even more significant. To clarify whether the original carbon in the material would affect its performance, we conducted relevant characterizations of the synthesized samples. As shown in Fig. S8,† the optical microscopy results showed that the carbon in NVPF-(002) was mixed with the NVPFs in an unbound state. Given this, we conducted conductivity tests on the cathode electrodes, and the results showed that the electrodes with NVPF and NVPF-(002) had the same conductivity (Table S8†). After forming the electrode with conductive carbon black, the small amount of carbon in the material would thus not affect the conductivity of the cathode electrode. Inorganic carbon usually plays a role in improving the conductivity of a cathode, thereby affecting the rate performance of the cell. Based on the above results, it could be inferred that the original carbon would not affect the rate performance of the cell. In addition, the performance of the full cell was evaluated by combining the NVPF-(002) cathode with a hard carbon anode (HC). Fig. 5a shows the charge–discharge curve of the NVPF-(002)||Na half-cell and Na||HC half-cell. Fig. 5b shows the schematic diagram of the NVPF-(002)||HC full cell. The charge–discharge curve of the full cell showed that

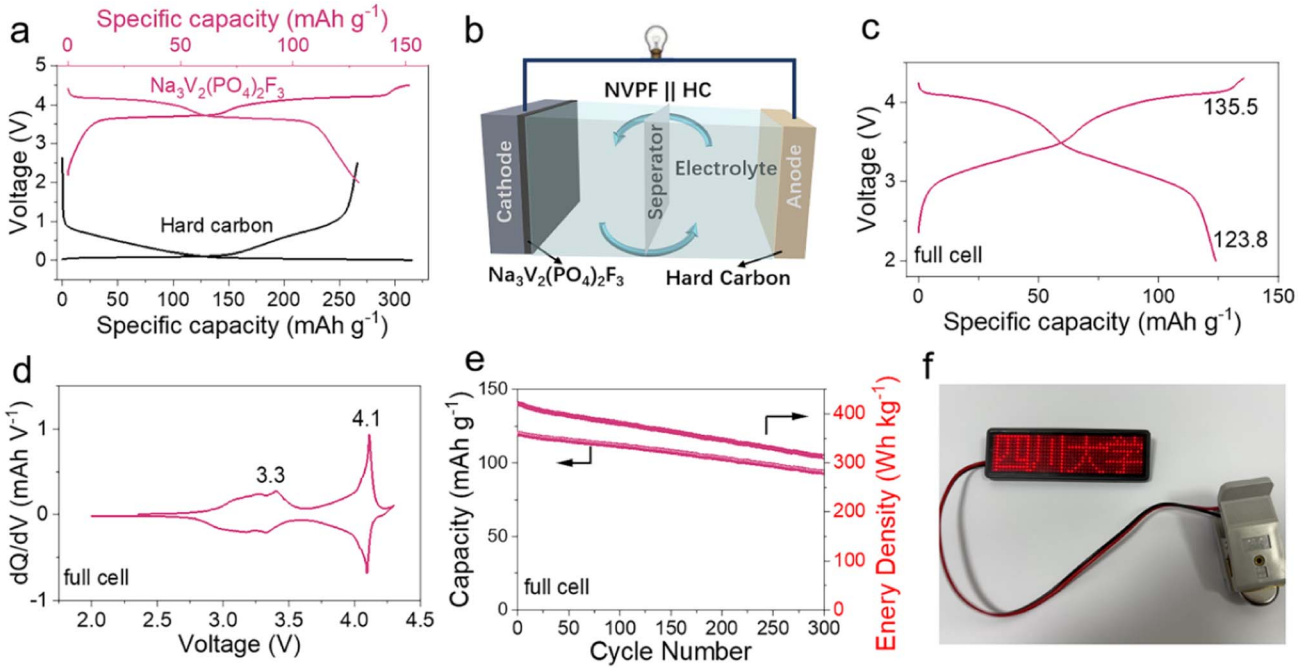

Fig. 5 (a) Charge–discharge curve of the NVPF-(002)||Na half-cell and Na||HC half-cell in the range 2.0–4.5 V. (b) Schematic diagram of the NVPF-(002)||HC full cell. (c) Charge–discharge curves and (d) dQ/dV curves of the NVPF-(002)||HC full cell in the range 2.0–4.3 V. (e) Cyclic performance curves at 100 mA g^{-1}. (f) Photo of the array of commercial LEDs used for displayed the Sichuan university logo powered by the NVPF-(002)||HC full cell.

it provided a reversible specific capacity of 123 mA h g^{-1} and energy density of 431 W h kg^{-1} (Fig. 5c). The dQ/dV curve displayed a charging and discharging platform at 3.3 V and 4.1 V, providing a median voltage of 3.44 V (Fig. 5d). Fig. 5e shows the cycle performance curve of the full cell over 300 cycles, demonstrating its good energy-storage stability. Fig. 5f shows that the NVPF||HC full cell could light up an array of 158 commercial red light-emitting diodes (LEDs), indicating its potential for commercialization.

First-principle calculations based on density functional theory and local density approximation were performed to explain the differences in the electrochemical performances of the NVPF cathodes. Based on the transfer process of Na^+, we calculated: (i) the adsorption energy of Na^+ on the crystal facets, corresponding to the desolvation and adsorption of Na^+ from the electrolyte onto the cathode facets; and (ii) the energy barrier for Na^+ to diffuse in different directions, corresponding to the migration of Na^+ in the cathode. Fig. 6a and S9† show schematic diagrams of the binding sites of Na^+ after desolvation from the electrolyte on the (001) crystal facet and (110) crystal facet, respectively. The adsorption energy calculation results (Fig. 6b) showed that the adsorption energy of Na^+ on the (001) crystal facet and on the (110) crystal facet was −1.14 and −0.60 eV, respectively. This indicates that the Na^+ desolvated from the electrolyte was more inclined to adsorb on the (001) crystal facet; in other words, there were more stable Na^+ storage sites on the (001) crystal facet. The differential charge density analysis (Fig. 6c and d) showed that more electrons gathered in the bonding area between Na and other atoms on the (001) crystal facet, indicating stronger interactions, thereby reducing the energy barrier of adsorption. The above results can explain the differences in Na-storage sites on the different crystal facets. After Na adsorbed on the crystal surface, it began to diffuse into the cathode, and so we calculated the diffusion energy barrier using the climbing-image nudged elastic band (CI-NEB) method. Fig. 6e and f show schematic diagrams of the diffusion path of Na^+ from different facets into the cathode. The calculation results show that the diffusion energy barrier of Na^+ from the (001) facet into the cathode was 0.43 eV (Fig. 6g), which was smaller than the diffusion energy barrier (0.66 eV) from the (110) facet into the cathode (Fig. 6h). Through detailed first-principles calculations for Na^+ adsorption, diffusion, and storage of the NVPFs, we theoretically determined that the exposed (002) crystal facet possessed more stable Na^+-storage sites, which resulted in a lower energy barrier during the Na^+-diffusion process.

Synchrotron X-ray absorption spectroscopy (XAS) was used to elucidate the essence of the performance differences in the NVPF samples. The appropriate K-space signal-to-noise ratio indicated that the collected data were of high quality (Fig. S10†). A pre-edge peak often appears in transition metal X-ray absorption near-edge structure (XANES) analysis, which is due to the transition from inner electrons to bound empty states. This pre-edge peak can be used as fingerprint information to qualitatively determine material information, because the formation conditions of the pre-edge are closely related to the structure of d-orbitals, and d-orbitals usually carry structural information, such as on the valence electrons, coordination

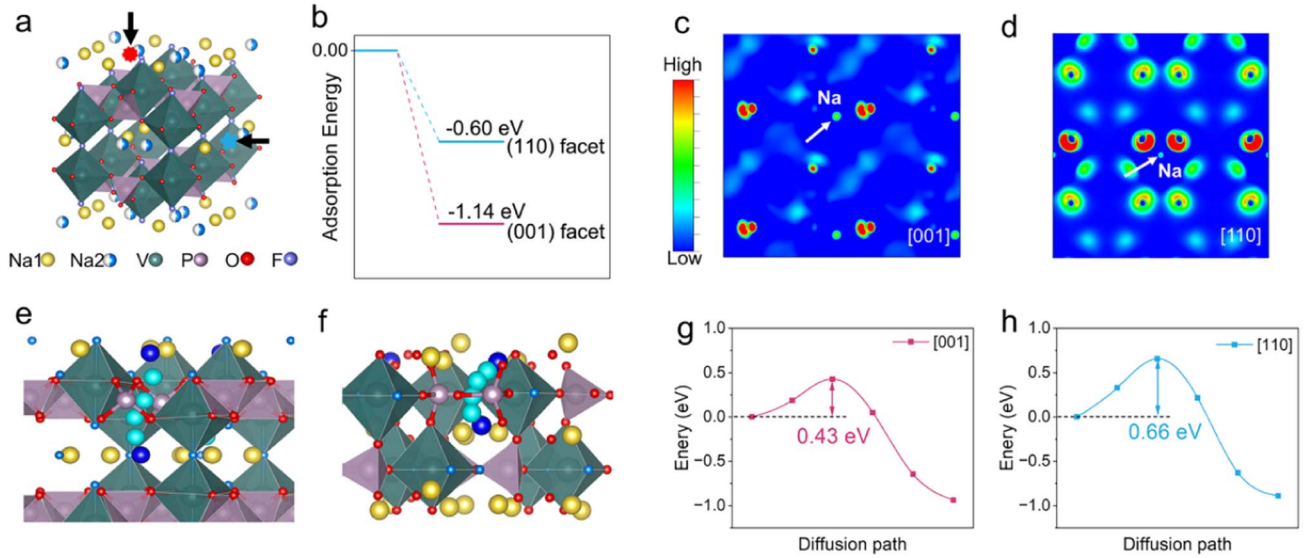

Fig. 6 (a) Schematic diagram of the Na^+-binding sites on different facets: (001) facet (red), (110) facet (blue). (b) Binding energies of the two sites. The differential charge density: (c) (001) facet, (d) (110) facet. Diffusion paths entering the cathode from different facets: (e) (001) facet, (f) (110) facet. Corresponding diffusion energy barrier: (g) (001) facet, (h) (110) facet.

number, and geometric structure (tetrahedron, octahedron, *etc.*). As shown in Fig. 7a, the similar pre-edge peaks of the two samples indicated similar local structures around the V. The pre-edge peak was used to measure the symmetry of the polyhedral structures. The appearance of the pre-edge peaks of the two samples indicated that the VO_4F_2 octahedron in the NVPFs was asymmetric because the bond lengths of the four O and two F with V were different. The results from the XRD refinement supported the above statement, as the bond lengths of the two V–F bonds and the four V–O bonds were indeed different, indicating a certain degree of deformation in the structure of the VO_4F_2 octahedron, which could explain the appearance of the pre-edge peak. The detailed bond length parameters are summarized in Tables S9 and S10.† The NVPFs consisted of a framework with VO_4F_2 octahedra and PO_4 tetrahedra, which endowed the NVPFs with good structural stability and inherent safety. The atomic oxidation state can be determined by the absorption edge position according to the reference material of the known oxidation state. The edge here was the same as that of the standard sample sodium vanadate phosphate (see the enlarged graph of the edge region in Fig. 7a), indicating that V existed in the form of V^{3+}. The Fourier transform spectra of the extended XAFS (EXAFS) curves (Fig. 7b) revealed the existence of a V–O peak and V–F peak between 1.3–2.1 Å, corresponding to the path from V to O and F in the VO_4F_2 octahedron, as shown in Fig. 7c and f. The similar peaks for the two samples indicated that they had a similar VO_4F_2 octahedron structure, which could provide a stable framework, and clarify the cycle stability of the two samples; the detailed differences are summarized in Table S11.† As shown in Fig. 7c and f for the interatomic distances from V to F, Na, O, and P in the succeeding layers, there was a difference in the radial distance between the two samples (Fig. 7b). The radial distance of NVPF-(002) was greater than that of NVPF, indicating an increase in distance from V to P and Na, which provides a broader Na^+ de-intercalation channel, and improved Na^+ de-intercalation kinetics, thereby improving the ability to charge–discharge quickly.

The electrochemical measurements also elucidated the remarkable performance of the NVPF-(002) cathode. The galvanostatic intermittent titration technique (GITT) was carried out to evaluate the Na^+-diffusion constant (D_{Na^+}) in the NVPF cathodes (Fig. 7d). D_{Na^+} changed with the state of charge (SOC) of the cathodes, and the trend of the scatter plot changed at 3.6 V and 4.0 V, which could be due to the intercalation of Na^+ into different sites, in which Na^+ could be inserted into Na_2 sites and Na_1 sites, respectively.[45,61] The GITT results showed that the NVPF-(002) cathode had a higher D_{Na^+} than NVPF, indicating faster Na^+ transport in the battery, which corresponded to the EXAFS results. The smaller band gap (E_g), the easier it is for electrons to be excited from the valence band to the conduction band, and the higher the intrinsic carrier concentration and conductivity.[62] The E_g results obtained from the diffuse reflectance spectrum here characterized by UV–vis showed that the NVPF-(002) sample (3.14 eV) had a smaller E_g than the NVPF sample (3.24 eV) (Fig. S11†). Next, cyclic voltammetry (CV) was used to evaluate the polarization and reversibility of the electrochemical reaction and electrode reaction, and the detailed oxidation–reduction potentials are comprehensively summarized in Table S12.† The results showed that reversible reactions occurred in both cathodes, and the NVPF-(002) cathode had a smaller voltage difference, indicating a weak polarization and better reversibility (Fig. 7e). The high intensity and sharpness of the peak indicated a fast diffusion rate of Na^+, which was consistent with the GITT results. The dQ/dV profiles for the NVPF cathodes were acquired by differentiating the charge–discharge curves of the 1st–1400th cycle (Fig. 7g). During charging, the oxidation potential of the NVPF cathode was higher than that of the NVPF-(002) cathode, indicating a greater

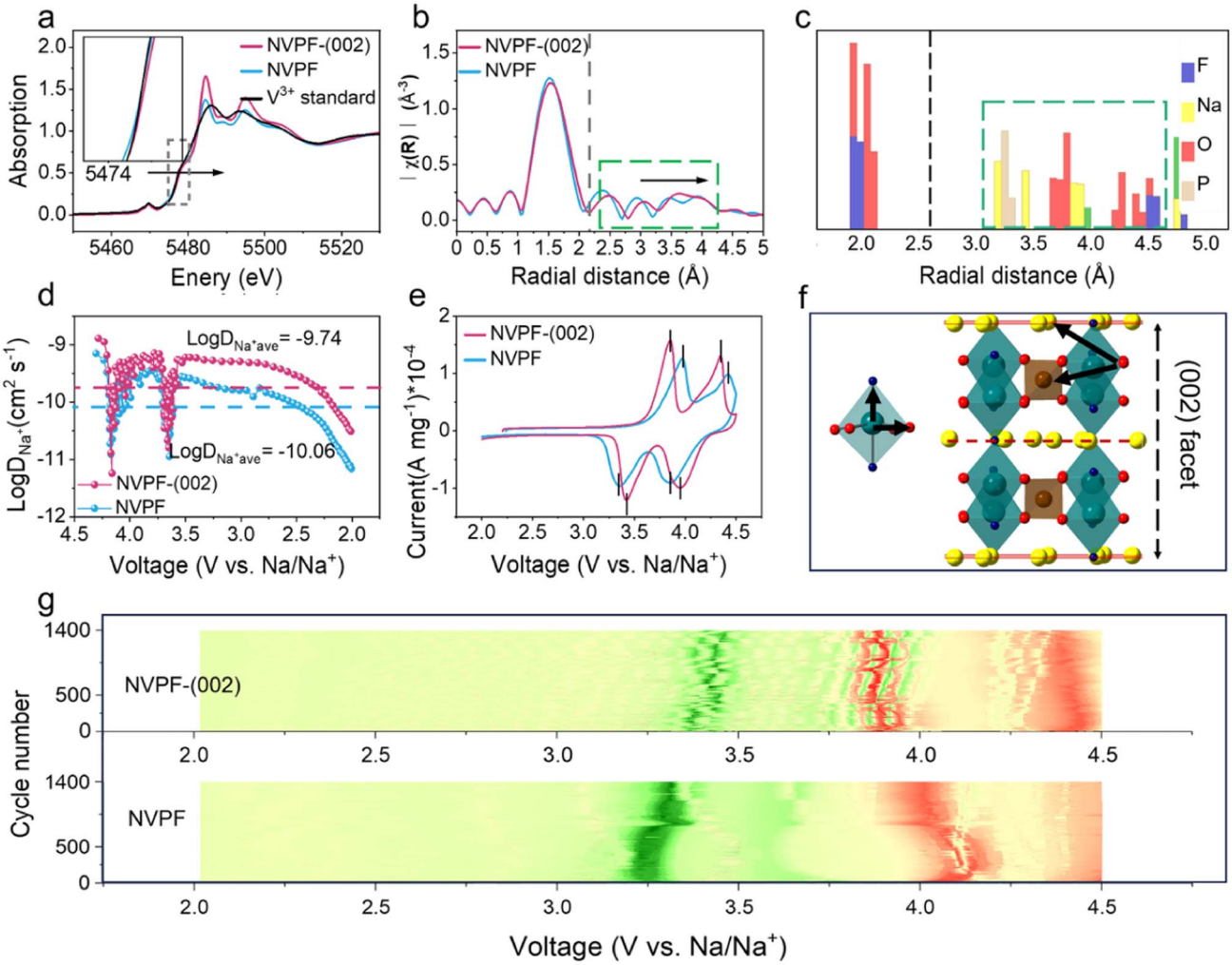

Fig. 7 (a) Normalized V K-edge XANES spectra of the NVPF samples; inset shows an enlarged graph of the edge region. (b) Fourier transform spectra of V K-edge of the NVPF samples from the EXAFS spectra. (c) Schematic diagram of the interatomic distances from V to F (blue), Na (yellow), O (red), and P (brown), with the first and subsequent layers distinguished by a black dashed line. (d) Na^+-diffusion coefficients at different discharge voltages of NVPF electrodes measured by GITT. (e) CV curves of NVPF electrodes at a sweep speed at 0.15 mV s^{-1}. (f) Schematic diagram of the radial distances from V (green) to F (blue), Na (yellow), O (red), P (brown). (g) Shift of the oxidation–reduction potential of NVPF electrodes during cycling (current density: 2C), charge (red), discharge (green).

resistance to Na^+ removal. The discharge of the NVPF-(002) cathode had a higher capacity contribution in the high-voltage region, while the NVPF capacity contribution was concentrated in the low-voltage region, indicating that the NVPF-(002) cathode could provide a higher discharge voltage and exhibit a higher energy density. The ion concentration difference caused by the imbalance of the electron- and ion-transport rates during the charge–discharge process is one of the reasons for the polarization phenomenon. The NVPF-(002) cathode had more (002) facets exposed, allowing for rapid Na^+ exchange at the interface, reducing the accumulation of Na^+ and reducing the concentration differences. Therefore, the NVPF-(002) cathode had a smaller oxidation–reduction potential difference, which was consistent with the CV results. This also indicated that the NVPF-(002) cathode had a more negligible voltage polarization during the charge–discharge process, which would be beneficial in the battery, for example, as it would have a higher energy efficiency (Fig. S7†).

Based on the above results and analysis, the Na^+-storage mechanism with different exposed crystal facets is proposed. Fig. S13† visually displays the Na^+ adsorption, migration, and storage of NVPF crystals at different charge–discharge current densities. It is easy to understand that at small current density, due to the longer charge–discharge time, Na^+ can slowly adsorb onto the surface of the cathode material, and finally reach the storage sites through diffusion and migration.[37,63] Therefore, at a low rate, NVPF and NVPF-(002) could be fully charged and discharged. At a high rate, the adsorption and migration of Na^+ on the crystal facets exposed to the electrolyte play a dominant role. Therefore, the NVPF-(002) cathode with more (002) active facets could quickly complete the adsorption, migration, and storage of Na^+, and exhibited a higher reversible capacity,

smaller polarization, and high energy density. In contrast, the NVPF cathode could not fully charge and discharge.

Conclusion

In summary, NVPFs with different exposure ratios of (002) active facets were synthesized by introducing/not introducing c-clusters. The (002) crystal facet area exposed to the electrolyte in the NVPF-(002) sample was 2.36 times that of the pure NVPF sample at the same volume. DFT calculations helped explain the above results and showed that c-clusters act as adsorbents during crystal growth, which could regulate the surface energy of different crystal facets and cause different crystal growth modes. The rate performance and long cycle testing results showed that the NVPF-(002) cathode with more (002) active facet exposed delivered a higher reversible capacity of 132 mA h g^{-1} and energy density of 482 W h kg^{-1}, and even 111 mA h g^{-1} and 391 W h kg^{-1} after 1400 cycles at 2C, with the performance advantages gradually increasing with the increase in current. First-principles calculations for Na^+ adsorption, diffusion, and storage of the NVPFs determined that the exposed (002) facets had more stable Na^+ storage sites, which resulted in a lower energy barrier during the Na^+ diffusion process. The XAS results indicated that the increase in radial distance from V to Na was one of the reasons for the increase in the Na^+-transport rate. The electrochemical mechanism analysis elucidated the essence of the performance differences of the NVPF samples. This research aimed to develop a way to promote the transmission process of Na^+ through the electrolyte/cathode interface from the perspective of crystal plane regulation, which may be expected to promote the commercial application of SIB cathodes.

Conflicts of interest

There are no conflicts to declare.

Acknowledgements

This work was supported by projects from the National Natural Science Foundation of China [No. U20A20145], State Key Laboratory of Polymer Materials Engineering [No. sklpme2020-3-02], Sichuan Provincial Department of Science and Technology [No. 2020YFG0022, No. 2022YFG0124], Dazhou Department of Science and Technology [No. 21ZDYF0001], Guangyuan Department of Science and Technology [No. 22ZDYF0047], Sichuan Province Science and Technology Achievement Transfer and Transformation Project [No. 21ZHSF0111], 2020 Strategic Cooperation Project between Sichuan University and Suining Municipal People's Government [No. 20221500008704170], the Open Project of State Key Laboratory of Environment-friendly Energy Materials [No. 20KFHG07], and Start-up funding of Chemistry and Chemical Engineering Guangdong Laboratory [No. 2122010]. The authors would like to thank eceshi (**https://www.eceshi.com**), Shiyanjia Lab (**https://www.shiyanjia.com**), and ceshigo (**https://www.ceshigo.com**) for providing technical support.

Notes and references

1 Z. Zhu, T. Jiang, M. Ali, Y. Meng, Y. Jin, Y. Cui and W. Chen, *Chem. Rev.*, 2022, **122**, 16610–16751.
2 Y. Li, F. Wu, Y. Li, M. Liu, X. Feng, Y. Bai and C. Wu, *Chem. Soc. Rev.*, 2022, **51**, 4484–4536.
3 T. Jin, H. Li, K. Zhu, P.-F. Wang, P. Liu and L. Jiao, *Chem. Soc. Rev.*, 2020, **49**, 2342–2377.
4 Y. Tian, G. Zeng, A. Rutt, T. Shi, H. Kim, J. Wang, J. Koettgen, Y. Sun, B. Ouyang, T. Chen, Z. Lun, Z. Rong, K. Persson and G. Ceder, *Chem. Rev.*, 2021, **121**, 1623–1669.
5 A. Rudola, C. J. Wright and J. Barker, *Energy Mater. Adv.*, 2021, **2021**, 9798460.
6 Q. Wang, J. Li, H. Jin, S. Xin and H. Gao, *InfoMat*, 2022, **4**, e12311.
7 Y.-F. Zhu, Y. Xiao, S.-X. Dou, Y.-M. Kang and S.-L. Chou, *eScience*, 2021, **1**, 13–27.
8 M. Wang, Q. Wang, X. Ding, Y. Wang, Y. Xin, P. Singh, F. Wu and H. Gao, *Interdisciplinary Materials*, 2022, **1**, 373–395.
9 Y. Xiao, Y.-F. Zhu, H.-R. Yao, P.-F. Wang, X.-D. Zhang, H. Li, X. Yang, L. Gu, Y.-C. Li, T. Wang, Y.-X. Yin, X.-D. Guo, B.-H. Zhong and Y.-G. Guo, *Adv. Energy Mater.*, 2019, **9**, 1803978.
10 X. Shen, Q. Zhou, M. Han, X. Qi, B. Li, Q. Zhang, J. Zhao, C. Yang, H. Liu and Y.-S. Hu, *Nat. Commun.*, 2021, **12**, 2848.
11 Y. Qi, Z. Tong, J. Zhao, L. Ma, T. Wu, H. Liu, C. Yang, J. Lu and Y.-S. Hu, *Joule*, 2018, **2**, 2348–2363.
12 H. Yi, M. Ling, W. Xu, X. Li, Q. Zheng and H. Zhang, *Nano Energy*, 2018, **47**, 340–352.
13 M. Xu, M. Liu, Z. Yang, C. Wu and J. Qian, *Acta Phys.-Chim. Sin.*, 2022, **39**, 2210043.
14 H. Fu, Y.-P. Wang, G. Fan, S. Guo, X. Xie, X. Cao, B. Lu, M. Long, J. Zhou and S. Liang, *Chem. Sci.*, 2022, **13**, 726–736.
15 C. Xu, J. Zhao, Y.-A. Wang, W. Hua, Q. fu, X. Liang, X. Rong, Q. Zhang, X. Guo, C. Yang, H. Liu, B. Zhong and Y.-S. Hu, *Adv. Energy Mater.*, 2022, **12**, 2200966.
16 C. Xu, W. Hua, Q. Zhang, Y. Liu, R. Dang, R. Xiao, J. Wang, Z. Chen, F. Ding, X. Guo, C. Yang, L. Yang, J. Zhao and Y.-S. Hu, *Adv. Funct. Mater.*, 2023, **33**, 2302810.
17 C. Xu, R. Xiao, J. Zhao, F. Ding, Y. Yang, X. Rong, X. Guo, C. Yang, H. Liu, B. Zhong and Y.-S. Hu, *ACS Energy Lett.*, 2022, **7**, 97–107.
18 C. Xu, J. Zhao, E. Wang, X. Liu, X. Shen, X. Rong, Q. Zheng, G. Ren, N. Zhang, X. Liu, X. Guo, C. Yang, H. Liu, B. Zhong and Y.-S. Hu, *Adv. Energy Mater.*, 2021, **11**, 2100729.
19 Q. Ni, Y. Bai, F. Wu and C. Wu, *Adv. Sci.*, 2017, **4**, 1600275.
20 P. Barpanda, L. Lander, S.-i. Nishimura and A. Yamada, *Adv. Energy Mater.*, 2018, **8**, 1703055.
21 L. N. Zhao, T. Zhang, H. L. Zhao and Y. L. Hou, *Mater. Today Nano*, 2020, **10**, 100072.
22 L. Zhu, H. Wang, D. Sun, Y. Tang and H. Wang, *J. Mater. Chem. A*, 2020, **8**, 21387–21407.
23 E. Wang, W. Xiang, R. Rajagopalan, Z. Wu, J. Yang, M. Chen, B. Zhong, S. X. Dou, S. Chou, X. Guo and Y.-M. Kang, *J. Mater. Chem. A*, 2017, **5**, 9833–9841.

24 X. Liu, G. Feng, Z. Wu, Z. Yang, S. Yang, X. Guo, S. Zhang, X. Xu, B. Zhong and Y. Yamauchi, *Chem. Eng. J.*, 2020, **386**, 123953.
25 E. Wang, M. Chen, X. Liu, Y. Liu, H. Guo, Z. Wu, W. Xiang, B. Zhong, X. Guo, S. Chou and S.-X. Dou, *Small Methods*, 2019, **3**, 1800169.
26 Z. Tian, Y. Zou, G. Liu, Y. Wang, J. Yin, J. Ming and H. N. Alshareef, *Advanced Science*, 2022, **9**, 2201207.
27 E. Wang, Y. Niu, Y.-X. Yin and Y.-G. Guo, *ACS Mater. Lett.*, 2021, **3**, 18–41.
28 Q. Zhao, S. Stalin and L. A. Archer, *Joule*, 2021, **5**, 1119–1142.
29 L. Zhu, L. Fu, K. Zhou, L. Yang, Z. Tang, D. Sun, Y. Tang, Y. Li and H. Wang, *Chem. Rec.*, 2022, **22**, e202200128.
30 S. Zhou, T. Mei, X. Wang and Y. Qian, *Nanoscale*, 2018, **10**, 17435–17455.
31 L. Qiu, M. Zhang, Y. Song, Z. Wu, Y. F. Zhu, J. Zhang, D. Wang, H. Y. Hu, H. W. Li, H. R. Liu, X. B. Jia, J. Peng, S. Chen, Z. Yang, Y. Xiao and X. Guo, *Carbon Energy*, 2022, **5**, 1–12.
32 Y. Xiao, P.-F. Wang, Y.-X. Yin, Y.-F. Zhu, Y.-B. Niu, X.-D. Zhang, J. Zhang, X. Yu, X.-D. Guo, B.-H. Zhong and Y.-G. Guo, *Adv. Mater.*, 2018, **30**, 1803765.
33 D. Wang, Y. Wu, C. Wu, Z. Ye, L. Yang, Y. Li, R. Dong, Z. Wu, Y. Sun, Y. Song and X. Guo, *ACS Appl. Mater. Interfaces*, 2022, **14**, 2711–2719.
34 F. Zuo, K. Bozhilov, R. J. Dillon, L. Wang, P. Smith, X. Zhao, C. Bardeen and P. Feng, *Angew. Chem., Int. Ed.*, 2012, **51**, 6223–6226.
35 M. Shi, G. Li, J. Li, X. Jin, X. Tao, B. Zeng, E. A. Pidko, R. Li and C. Li, *Angew. Chem., Int. Ed.*, 2020, **59**, 6590–6595.
36 M. Zhou, S. Guo, J. Li, X. Luo, Z. Liu, T. Zhang, X. Cao, M. Long, B. Lu, A. Pan, G. Fang, J. Zhou and S. Liang, *Adv. Mater.*, 2021, **33**, 2100187.
37 X. Xu, R. Zhao, B. Chen, L. Wu, C. Zou, W. Ai, H. Zhang, W. Huang and T. Yu, *Adv. Mater.*, 2019, **31**, 1900526.
38 T. Wei, P. Ding, T. Wang, L.-M. Liu, X. An and X. Yu, *ACS Catal.*, 2021, **11**, 14669–14676.
39 F. Fu, G.-L. Xu, Q. Wang, Y.-P. Deng, X. Li, J.-T. Li, L. Huang and S.-G. Sun, *J. Mater. Chem. A*, 2013, **1**, 3860.
40 J. Zhao, L. Mu, Y. Qi, Y.-S. Hu, H. Liu and S. Dai, *Chem. Commun.*, 2015, **51**, 7160–7163.
41 L. H. B. Nguyen, T. Broux, P. S. Camacho, D. Denux, L. Bourgeois, S. Belin, A. Iadecola, F. Fauth, D. Carlier, J. Olchowka, C. Masquelier and L. Croguennec, *Energy Storage Mater.*, 2019, **20**, 324–334.
42 Y. Qi, L. Mu, J. Zhao, Y.-S. Hu, H. Liu and S. Dai, *Angew. Chem., Int. Ed.*, 2015, **54**, 9911–9916.
43 J. Olchowka, L. H. B. Nguyen, T. Broux, P. Sanz Camacho, E. Petit, F. Fauth, D. Carlier, C. Masquelier and L. Croguennec, *Chem. Commun.*, 2019, **55**, 11719–11722.
44 F. Sauvage, E. Quarez, J. M. Tarascon and E. Baudrin, *Solid State Sci.*, 2006, **8**, 1215–1221.
45 J.-Z. Guo, P.-F. Wang, X.-L. Wu, X.-H. Zhang, Q. Yan, H. Chen, J.-P. Zhang and Y.-G. Guo, *Adv. Mater.*, 2017, **29**, 1701968.
46 A. A. McConnell, J. S. Aderson and C. N. R. Rao, *Spectrochim. Acta, Part A*, 1976, **32**, 1067–1076.
47 J. Zhang, D. Wang, D.-M. Zhang, Q.-L. Zhang, S.-M. Wan, D.-L. Sun and S.-T. Yin, *Acta Phys. Sin.*, 2013, **62**, 097802.
48 R. Marassi and F. Nobili, in *Encyclopedia of Electrochemical Power Sources*, ed. J. Garche, Elsevier, Amsterdam, 2009, pp. 769–789, DOI: **10.1016/B978-044452745-5.00072-1**.
49 L. Zhu, Q. Zhang, D. Sun, Q. Wang, N. Weng, Y. Tang and H. Wang, *Mater. Chem. Front.*, 2020, **4**, 2932–2942.
50 W. Song, X. Cao, Z. Wu, J. Chen, Y. Zhu, H. Hou, Q. Lan and X. Ji, *Langmuir*, 2014, **30**, 12438–12446.
51 Z. Liu, B. Lv, D. Wu, Y. Sun and Y. Xu, *Eur. J. Inorg. Chem.*, 2012, **2012**, 4076–4081.
52 S. A. Claridge, A. W. Castleman, S. N. Khanna, C. B. Murray, A. Sen and P. S. Weiss, *ACS Nano*, 2009, **3**, 244–255.
53 Y. Xia, Y. Xiong, B. Lim and S. E. Skrabalak, *Angew. Chem., Int. Ed.*, 2009, **48**, 60–103.
54 J. Liu, W. Shi, B. Ni, Y. Yang, S. Li, J. Zhuang and X. Wang, *Nat. Chem.*, 2019, **11**, 839–845.
55 J. Li and F. L. Deepak, *Chem. Rev.*, 2022, **122**, 16911–16982.
56 L. Shan, Y. Wang, S. Liang, B. Tang, Y. Yang, Z. Wang, B. Lu and J. Zhou, *InfoMat*, 2021, **3**, 1028–1036.
57 Z.-J. Sui, Y.-A. Zhu, P. Li, X.-G. Zhou and D. Chen, in *Advances in Chemical Engineering*, ed. G. B. Marin, Academic Press, 2014, vol. 44, pp. 61–125.
58 Y. Wang, W. Qiu, E. Song, F. Gu, Z. Zheng, X. Zhao, Y. Zhao, J. Liu and W. Zhang, *Natl. Sci. Rev.*, 2017, **5**, 327–341.
59 B. Hinnemann, P. G. Moses, J. Bonde, K. P. Jørgensen, J. H. Nielsen, S. Horch, I. Chorkendorff and J. K. Nørskov, *J. Am. Chem. Soc.*, 2005, **127**, 5308–5309.
60 H. Yi, L. Lin, M. Ling, Z. Lv, R. Li, Q. Fu, H. Zhang, Q. Zheng and X. Li, *ACS Energy Lett.*, 2019, **4**, 1565–1571.
61 Y.-U. Park, D.-H. Seo, H. Kim, J. Kim, S. Lee, B. Kim and K. Kang, *Adv. Funct. Mater.*, 2014, **24**, 4603–4614.
62 Z.-Y. Gu, J.-Z. Guo, J.-M. Cao, X.-T. Wang, X.-X. Zhao, X.-Y. Zheng, W.-H. Li, Z.-H. Sun, H.-J. Liang and X.-L. Wu, *Adv. Mater.*, 2022, **34**, 2110108.
63 P. Gao, Y.-Y. Zhang, L. Wang, S. Chen, Y. Huang, X. Ma, K. Liu and D. Yu, *Nano Energy*, 2017, **32**, 302–309.